Comparative Evaluation of Cast Aluminum Alloys for Automotive Cylinder Heads: Part I—Microstructure Evolution

SHIBAYAN ROY, LAWRENCE F. ALLARD, ANDRES RODRIGUEZ, THOMAS R. WATKINS, and AMIT SHYAM

The present study stages a comparative evaluation of microstructure and associated mechanical and thermal response for common cast aluminum alloys that are used for manufacturing automotive cylinder heads. The systems considered are Al-Cu (206-T6), Al-Si-Cu (319-T7), and Al-Si (356-T6, A356-T6, and A356 + 0.5Cu-T6). The focus of the present manuscript is on the evaluation of microstructure at various length scales after aging, while the second manuscript will deal with the mechanical and thermal response of these alloys due to short-term (aging) and long-term (pre-conditioning) heat treatments. At the grain-scale, the Al-Cu alloy possessed an equiaxed microstructure as opposed to the dendritic structure for the Al-Si-Cu or Al-Si alloys which is related to the individual solidification conditions for these alloy systems. The composition and morphology of intermetallic precipitates within the grain and at the grain/dendritic boundary are dictated by the alloy chemistry, solidification, and heat treatment conditions. At the nanoscale, these alloys contain various metastable strengthening precipitates (GPI and θ'' in Al-Cu alloy, θ' in Al-Si-Cu alloy, and β' in Al-Si alloys) with varying size, morphology, coherency, and thermal stability.

DOI: 10.1007/s11661-017-3985-1

I. INTRODUCTION

APPLICATION of precipitation-strengthened cast aluminum alloys to replace cast iron components in the passenger vehicle power trains, *e.g.*, cylinder heads or engine blocks, has been a signature light-weighting achievement in the automotive industry.[1,2] The most commonly used cast alloys for cylinder head applications are those from the Al-Si-Cu (*e.g.*, 319 or A319) or Al-Si (*e.g.*, 356 or A356) systems.[3] The compositions of these alloys are optimized for fabricating complex components with adequate mechanical performance, castability, and cost. Silicon in these alloy systems provides required fluidity, hot tear resistance, and desired mold feeding characteristics.[2]

Numerous studies have been performed that reveal aspects of structure evolution at various length scales in these alloy systems. Some of these studies were aimed to understand the effect of solidification conditions on the dendritic structure evolution and related feature size variations.[4–8] On the microstructural level, the roles of various alloying elements, either on the formation of solidification defects such as shrinkage porosity[9–11] or the brittle intermetallics within the interdendritic regions[12–17] have attained the most interest. For example, crystal structure and crystallization behavior of Fe-containing intermetallics,[18–20] their formation mechanisms,[21] and three-dimensional morphology[22,23] have been studied. The role of certain elements (*e.g.*, Mn)[24–28] or specialized heat treatment[29] that cause structural and morphological transformations between different Fe-intermetallics (acicular β to irregular or 'Chinese script' α) has also been studied in detail. Such transformations are found desirable in relation to porosity formation and the castability for the Al-Si and Al-Si-Cu alloys.

The modification of eutectic Si phase morphology through various trace element additions, *e.g.*, Na, P, Sr[30–34] as well as Sb, Bi, Sr,[35] the associated mechanisms[36] and effects of such modification on the tensile properties of cast alloys[37] has also been well-reported for Al-Si-Cu or Al-Si alloys. Furthermore, the structure, morphology, and composition of nanoscale strengthening precipitates such as β'-Mg_2Si or Q',[38–40] their evolution pathways over the aging heat treatment,[14,41,42] and role of alloying elements in modifying these nanoscale precipitates[40,43–45] have added to the knowledgebase for the Al-Si alloys. The Al-Cu alloy systems, on the other hand, have been studied as model systems to understand the characteristics of nanoscale strengthening θ'- Al_2Cu precipitates.[46–49] Lesser effort has been expended toward the characterization of microstructural features such as equiaxed grains or dendritic structures and the coarse intermetallics for this system.

SHIBAYAN ROY is with the Materials Science and Technology Division, Oak Ridge National Laboratory, Oak Ridge, TN, 37831, and also with the Materials Science Centre, Indian Institute of Technology, Kharagpur, 721302, India. Contact e-mail: royshiba@gmail.com, shibayan@matsc.iitkgp.ernet.in LAWRENCE F. ALLARD, THOMAS R. WATKINS, and AMIT SHYAM are with Materials Science and Technology Division, Oak Ridge National Laboratory. ANDRES RODRIGUEZ is with Nemak, S.A., 66000, García, N.L., Mexico.

Manuscript submitted May 18, 2016.
Article published online March 6, 2017

A careful scrutiny of this vast knowledgebase for cast Al-Cu, Al-Si-Cu, or Al-Si alloys reveals two important aspects which warrant further exploration. First, the structural information about these alloy systems is quite scattered and generally available at only one (either micro or nano) length scale. Just a few studies have attempted to develop a comprehensive structural understanding from the grain-scale all the way to the nanoscale features.[50] More importantly, any comparison of the structural features (at all length scales) between these alloy systems is not available till date. Such study would be helpful to design automotive cylinder heads with superior property combinations.[51]

The present study attempts to develop a fundamental knowledgebase for five common aluminum alloys that are generally used in casting automotive cylinder heads; three of them belong to Al-Si system (356-T6, A356-T6 and A356 + 0.5Cu-T6), while the other two are from the Al-Si-Cu (319-T7) and Al-Cu (206-T6) systems. In order to replicate the alloy microstructures in the combustion chamber region of cylinder heads, the cast blanks were extracted from those locations in a gravity die wedge cast ingot that contained a pre-specified grain size (~90 μm for 206 alloy) or secondary dendrite arm spacing, SDAS (~30 μm, for 319, 356, A356, and A356 + 0.5Cu alloys).

In the first part, that is the current manuscript, we investigate the structure evolution in these five alloys at various length scales using microscopy and X-ray diffraction techniques in the as-aged condition. In the second part, mechanical and thermal properties of these alloys as a function of different heat treatment schedules are reported and discussed.[72]

II. EXPERIMENTAL PROCEDURE

A. *Materials and Heat Treatment*

Five different alloys were used in the present study, one each from Al-Si-Cu (319) and Al-Cu (206) systems and three from the Al-Si system (356, A356, and A356 + 0.5Cu). Composition of these alloys (Table I) was determined *via* inductively coupled plasma optical emission spectrometry (ICP-OES) and inductively coupled plasma mass spectroscopy (ICP-MS) techniques (for alloying elements in wt pct and impurity contents up to ppm detection level, respectively). The alloys were melted at a temperature above 1073 K (800 °C) and cast into sand molds with varying thickness (gravity die wedge casting). Subsequently, small blanks of dimension 6.5″ (length) × 0.75″ (width) × 0.75″ (thickness) were extracted from identical regions of the wedge cast ingots such that the secondary dendrite arm spacing (SDAS) was ~25 μm for Al-Si-Cu (319) alloy and ~30 μm for the three Al-Si (356, A356, and A356 + 0.5Cu) alloys. It is important to note that the microstructure of the alloy ingots can vary considerably due to varying thickness in wedge casting at different locations since the cooling rate during solidification is sensitive to alloy composition (Al-Si-Cu *vs.* Al-Si alloys).[6,7,52–54]

These blanks were then solution-treated as per the schedule provided in Table II and water quenched to 363 K (90 °C). The solution-treated and quenched alloy blanks were subsequently aged at various temperatures (Table II) up to 5 hours which yielded a final T6 condition for Al-Cu (206) and Al-Si alloys (356, A356, A356 + 0.5Cu) and T7 condition for Al-Si-Cu (319) alloy.[55] Solutionizing and aging treatments were carried out in a forced convection oven. The aged specimens were air-cooled to room temperature after aging.

B. *Optical and SEM Characterization for Microstructural Features*

As shown in Figure 1, the faces of the blanks originally extracted from the cast ingot are named with the following convention: X-face⊥X-direction (length direction of the blanks), Y-face⊥Y-direction (width direction of the billet), and Z-face⊥Z-direction (thickness direction of the billet). The observation surfaces for optical and electron microscopy were first metallographically polished up to 2500 grit SiC paper and finished with 1 μm diamond paste. The polished surfaces were then etched using Keller's solution (1.5 pct HCl, 2.5 pct HNO_3, and 1 pct mL HF by volume in water) by immersing the specimens for 10 seconds. Microstructural characterization was performed on the specimens ONLY in the as-aged condition. Optical micrographs were collected from these three faces in differential interference contrast (DIC) mode*. Scanning electron micrographs (SEM)** were recorded in backscatter electron (BSE) mode from the horizontal surfaces of the blanks (from Z-face with image normal‖Z-direction). Compositional analysis of various microstructural features was also carried out from the Z-face using energy-dispersive spectroscopy technique in the SEM (SEM–EDS). For SEM and EDS studies, an accelerating voltage of 20 kV and effective working distance of 13 mm were used.

The size of various microstructural features (equiaxed grains or secondary dendrites plus coarse intermetallics) was estimated by linear intercept method† from the optical (from X-, Y-, and Z-faces) and SEM (from Z-face) micrographs. Several vertical and horizontal lines were drawn to obtain statistical reliability with 95 pct confidence interval. From the measured values, a cumulative distribution (in terms of number fractions) of intercept lengths was obtained and the weighted

*Olympus BX51M, Olympus.

**HITACHI® S4800 FE-SEM, Japan.

†ImageJ® developed by National Institute of Health.

Table I. Detailed Compositions (in wt pct) of Various Alloys (Only the Major Alloying Elements Are Mentioned, Minor Elements in ppm Level Includes Pb, Na, Sr, P, B, Ca, *etc.*)

Alloy Condition	Si	Cu	Fe	Mn	Mg	Zn	Ti	Al (Balance)
206	0.17	5	0.15	0.25	0.32	0.005	0.021	93.88
319	8.3	3.17	0.68	0.39	0.34	0.31	0.1	86.62
356	7.21	0.14	0.39	0.25	0.37	0.17	0.19	91.28
A356	7.32	0.01	0.18	0.06	0.4	0.005	0.16	91.87
A356 + 0.5Cu	7.46	0.44	0.14	0.08	0.34	0.01	0.16	91.37

Table II. Solution Treatment and Subsequent Aging Conditions for Various Alloys

Alloy	Temper Designation	Solution Treatment Condition	Aging Conditions
206	T6	803 K (530 °C) for 5 h	463 K (190 °C) for 5 h
319	T7	763 K (490 °C) for 5 h	513 K (240 °C) for 5 h
356	T6	783 K (510 °C) for 5 h	483 K (210 °C) for 5 h
A356	T6	803 K (530 °C) for 5 h	433 K (160 °C) for 5 h
A356 + 0.5Cu	T6	803 K (530 °C) for 5 h	433 K (160 °C) for 5 h

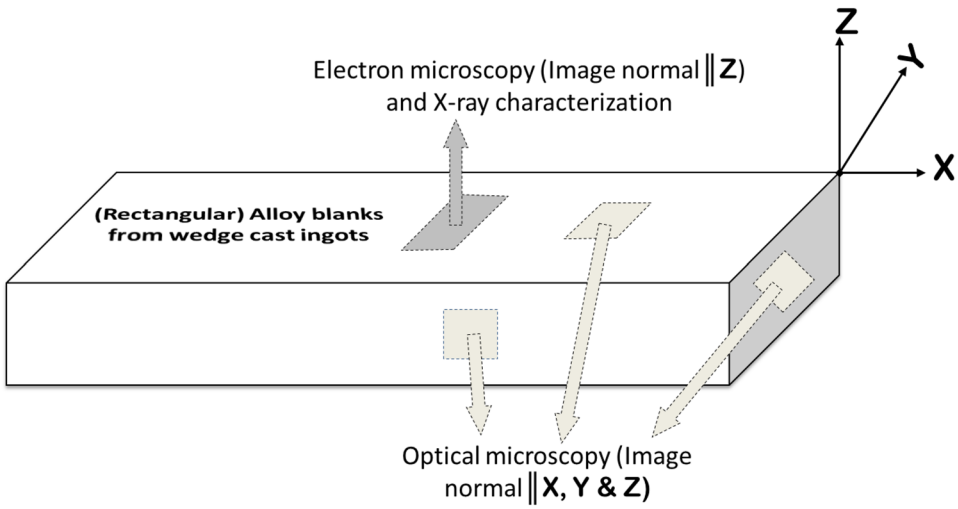

Fig. 1—Schematic showing the scheme of microstructural and X-ray-based characterizations.

average plus corresponding error value was calculated. Average linear intercepts were finally converted to equivalent feature sizes (equiaxed grain sizes or secondary dendrite sizes) by multiplying with a stereological factor of 1.56 as per the ASTM standard E112-96.

C. *Nanostructural Characterization*

The nanostructures of the as-aged alloys (up to the atomic level) were characterized using electron-transparent thin foil specimens prepared by electropolishing and/or argon ion beam milling techniques. Electropolished foils were prepared from 3-mm disks (core-drilled from 100 μm slices originally cut from the bulk alloy blanks) using a Tenupol double-jet system with 25 pct HNO_3-75 pct methanol electrolyte chilled to 260 K (−13 °C).[56] Some foils were further thinned down (as needed for electron transparency), using a Fischione 1010 argon ion mill, with opposing Ar beams operated at 3 kV, 5 mA, and 12 deg tilt angle, typically for 30 minutes or less. The sample was chilled with liquid nitrogen during milling to prevent microstructural artifacts resulting from heat build-up in the foil.

The electron microscopy for nanostructural characterization of the as-aged alloys was carried out with a JEOL 2200FS (scanning) transmission electron microscope (STEM), operated in scanning mode with the capability to record simultaneous bright-field (BF) and high-angle annular dark-field (HAADF) images. The instrument was equipped with a CEOS GmbH (Heidelberg, Germany) aberration corrector on the probe-forming lenses that routinely achieved 0.07 nm resolution in HAADF mode, with a probe convergence semi-angle of 26.5 deg, and detector inner angle of 110 deg. HAADF images were recorded with the electron beam in either an $\langle 001 \rangle_{Al}$ or a $\langle 110 \rangle_{Al}$ zone axis orientation. Only the $\langle 001 \rangle_{Al}$ images were used for size and number density measurement of the nanoscale precipitates within any

given microstructural area. The measurement scheme uses linear intercepts and is similar to that used for the measurement of features in the SEM micrographs (described in more detail in Section II–B of Part II of this paper). As described later, the primary strengthening precipitate in the Cu-based alloys is plate-shaped θ'' or θ', where the plates align along the three $\{001\}_{Al}$ cube faces of the FCC-Al structure.[57] For the Al-Si alloys, the nanoscale precipitate is rod-shaped β'-Mg_2Si with circular cross section and $\langle 001\rangle_{Al}$ as the preferred growth direction.[40]

D. *X-ray Characterization*

Phase identification of the as-aged alloys was performed by X-ray diffraction[‡] using a line detector. The horizontal surfaces (Z-faces) of the billets were placed on the center of rotation of the $\theta-2\theta$ goniometer using a dial gauge probe, precise to ± 10 μm. Using Cu K_α radiation (λ = 1.541874 Å), XRD patterns were collected in ~3 hours with a continuous scan mode from 5–70 deg 2θ and a step size of 0.0167 deg. All the X-ray scans used ¼ deg incident slits and ½ deg incident and receiving anti-scatter slits. Incident and receiving 0.25 deg Soller slits and a receiving Ni filter were also used. Search match was conducted using the Jade®[§] and/or HighScore Plus®[§§] softwares with the PDF database[¶].

[‡]X'Pert Pro MPD $\theta-\theta$ goniometer with Xcelerator detector, PANalytical B.V., Amelo, The Netherlands.

[§]Jade (2012), version 9.4.5 (computer software), Materials Data Inc., Livermore, CA 94550.

[§§]High Score Plus (2012), version 3.0e(3.0.5) (computer software), PANalytical B.V., Amelo, The Netherlands.

[¶]ICDD, PDF-4+ 2014, International Centre for Diffraction Data, Newtown Square, PA.

III. RESULTS AND DISCUSSIONS

A. *Microstructure and Phases of the As-aged Alloys*

1. *Optical characterization*

Figure 2 shows the virtual cuboids assembled from the optical micrographs that were collected from the three faces (image normal perpendicular to either X, Y, or Z directions) of the as-aged alloy blanks. The Al-Cu alloy (206) microstructure is composed of equiaxed α-Al grains with nearly equivalent size and distribution on all three faces (marked in Figure 2(a) left). The average grain size in the 206 alloy is ~90 μm, while the distribution shows an extended tail toward higher grain size values (>150 μm, Figure 2(a) right). The equiaxed grain structure in this alloy is a direct consequence of grain refinement during solidification through the addition of Ti-B master alloy.[2] The microstructure also contains various intermetallic particles at the α-Al grain boundaries. In the case of the Al-Si-Cu (319) or Al-Si (356, A356 and A356 + 0.5Cu) alloys, the microstructure consists of α-Al dendrites which are again marked on each face of the respective unit cubes in Figures 2(b) through (e) left. Similar to the 206 alloy, the dendritic structures for these four alloys are homogeneous on the three faces with interdendritic regions containing various intermetallic phases.

Fig. 2—Optical micrographs obtained using differential interference contrast (DIC) technique from different faces of the cast blanks (assembled in the form of a virtual cuboid on the left) and corresponding microstructural size distribution (right) for (*a*) 206, (*b*) 319, (*c*) 356, (*d*) A356, and (*e*) A356 + 0.5Cu alloys. Various important microstructural features (α-Al dendrites, interdendritic regions, large precipitates in the interdendritic regions, *etc.*) are marked in the optical images. The selected regions within the dotted lines indicate primary and secondary dendrites on each face.

The identification and size measurement for the primary dendrites in Al-Si-Cu or Al-Si alloys were problematic even when a statistically significant number (~30 optical micrographs of different magnifications) was analyzed. The secondary dendrites also displayed a large spread making quantitative comparison among the four alloys difficult (Table III). Nonetheless, the overall microstructure (secondary dendrite size) appears finer for 319 and A356 + 0.5Cu (~46–47 μm, Figures 2(b) and (e)) as compared to 356 and A356 (~60 μm, Figures 2(c) and (d)). As already explained, these cast blanks were extracted from the wedge cast ingots wherein the secondary dendrite arm spacing (SDAS) was ~25 μm for Al-Si-Cu alloy and ~30 μm for the three Al-Si alloys. Even for the same mold conditions (temperature and location) and SDAS, secondary dendrite size can vary considerably at different locations in wedge cast alloy ingot since the cooling rate during solidification varies as per the alloy compositions (Al-Si-Cu *vs.* Al-Si alloys).[6,7,52–54] The higher Si content in the Al-Si-Cu alloy (8.1 wt pct in 319) as compared to Al-Si alloys (7.15–7.3 wt pct for 356 or A356) increases the amount of solute that interferes with the growth of the dendrite, thus producing a finer microstructure for the former alloy.[8] Comparatively finer secondary dendrites in A356 + 0.5Cu (~7.3 wt pct Si) among the three Al-Si alloys are possibly because of the stronger refining effect from the additional Cu in the composition.[58]

2. *SEM–EDS characterization*

The 206 alloy contains blocky primary eutectic Al_2Cu intermetallics at the grain boundaries (Figure 3). These particles are mostly characterized with irregular morphology and their sizes vary in the range of 2–6 μm. The microstructure also contains elongated Fe-rich precipitates ~10–20 μm length and ~1.5 μm width without Mn. The elongated morphology and the presence of Cu suggest that these are ω-Al_7Cu_2Fe precipitates.[21,22,27] It

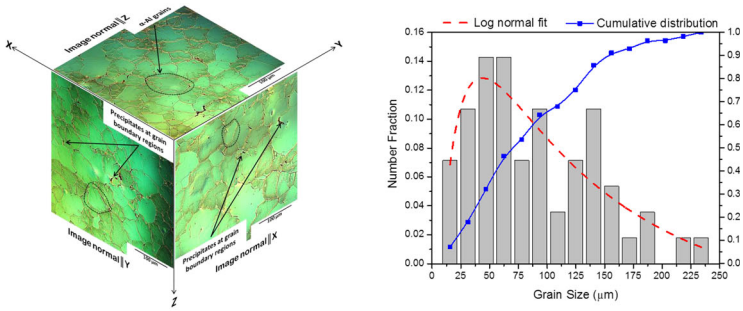
Image normal ∥ Z
Image normal ∥ Y
Image normal ∥ X
Precipitates at grain boundary regions
Precipitates at grain boundary regions
Log normal fit
Cumulative distribution
Number Fraction
Grain Size (μm)

(a)

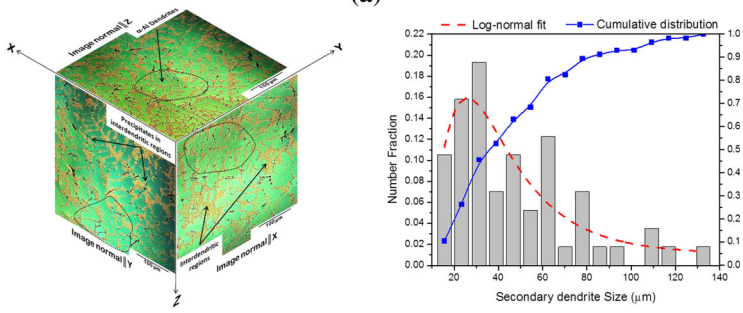
Image normal ∥ Z
Image normal ∥ Y
Image normal ∥ X
Precipitates in interdendritic regions
Interdendritic regions
Log-normal fit
Cumulative distribution
Number Fraction
Secondary dendrite Size (μm)

(b)

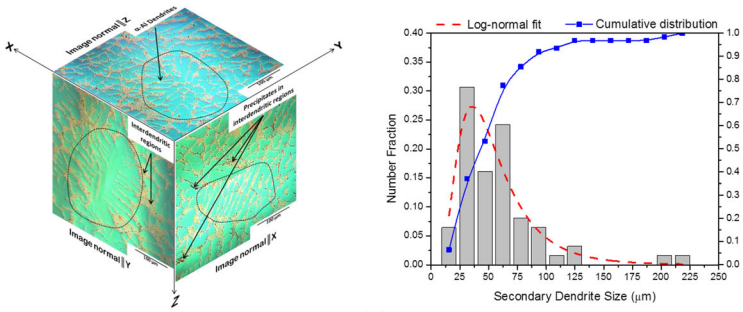
Image normal ∥ Z
Image normal ∥ Y
Image normal ∥ X
Interdendritic regions
Precipitates in interdendritic regions
Log-normal fit
Cumulative distribution
Number Fraction
Secondary Dendrite Size (μm)

(c)

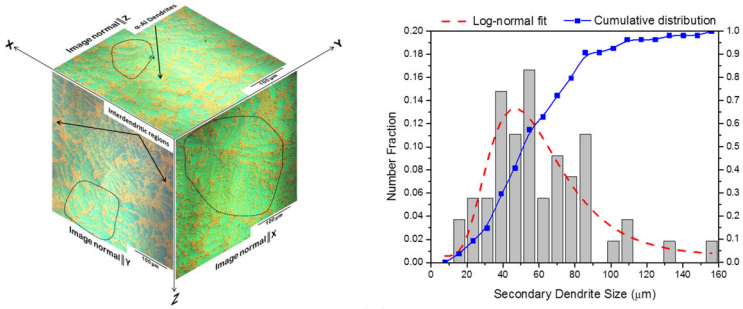
Image normal ∥ Z
Image normal ∥ Y
Image normal ∥ X
Interdendritic regions
Log-normal fit
Cumulative distribution
Number Fraction
Secondary Dendrite Size (μm)

(d)

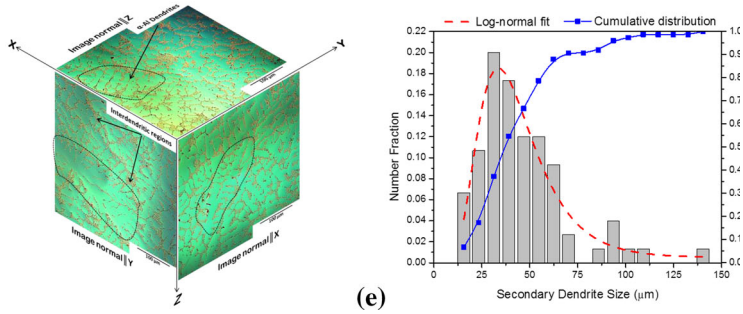
Image normal ∥ Z
Image normal ∥ Y
Image normal ∥ X
Interdendritic regions
Log-normal fit
Cumulative distribution
Number Fraction
Secondary Dendrite Size (μm)

(e)

Table III. Grain or Secondary Dendrite and Eutectic Si Sizes for Various Alloys. The Error Is Expressed as the Standard Deviation of the Measured Dataset

Alloy	Grain Size/Secondary Dendrite Size (μm)	Eutectic Si	
		Width (μm)	Length (μm)
206	89.7 ± 3.7		
319	47.2 ± 2.1	3.9 ± 2.4	6.1 ± 3.7
356	58.1 ± 4.3	1.7 ± 0.8	2.8 ± 1.9
A356	60.2 ± 3	1.94 ± 1.2	2.96 ± 1.75
A356 + 0.5Cu	46 ± 2.45	2.35 ± 1.3	2.82 ± 1.75

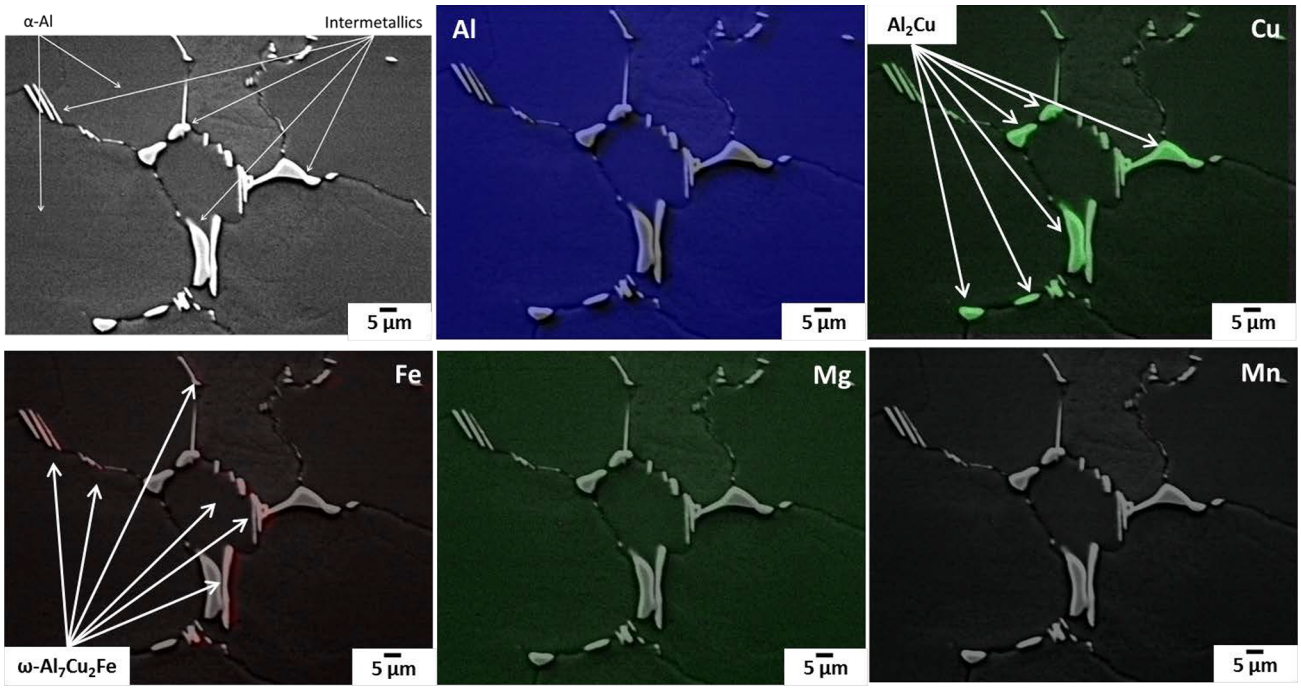

Fig. 3—BSE micrographs (top, left) and elemental maps (superimposed with BSE image) obtained from EDS scan from corresponding area showing the distribution of various intermetallic precipitates in the microstructure of cast 206 alloy. The elements are inscribed in the corresponding maps.

appears surprising considering the Mn concentration (0.25 wt pct) in 206 being even higher than Fe (0.15 wt pct) which instead should produce 'Chinese script' α-$Al_{15}(Fe,Mn)_3(Si,Cu)_2$ phase after solidification. The ω-Al_7Cu_2Fe phase may, however, form from the solid-state transformation of α-$Al_{15}(Fe,Mn)_3(Si,Cu)_2$ during solution treatment.[18]

The microstructure for the 319 alloy is characterized by eutectic Si particles in the interdendritic region alongside various intermetallic phases and α-Al dendrites (Figure 4(a)). The eutectic Si particles are nodular and usually ~3–5 μm in size suggesting adequate modification by trace elements (Na, Sr, P, Ca *etc.*) present in the composition.[30–33] The intermetallics within the interdendritic regions appear in two different morphologies: either as elongated plates with high aspect ratio or blocky and spherical with low aspect ratio (Figures 4(c), (d)). The plate-shaped intermetallics are β-Al_5FeSi or more precisely, β-$Al_9Fe_2Si_2$[29] with varying size and aspect ratio (~10–20 μm in length, while >1 μm in width).[22] The blocky intermetallics, on the other hand, are finer (~2–5 μm) and contain Fe plus Si and Mn (α-$Al_8(Fe,Mn)_2Si$).[19,20,25] The α-$Al_8(Fe,Mn)_2Si$ precipitates are described as the 'Chinese script' intermetallics for their complex morphology as shown in Figure 4(b). Some of these blocky and/or spherical particles are also observed without any ternary elements such as Mn, Mg, or Si. These are the primary eutectic Al_2Cu.[12–14] Finally, few of the Cu and Mg-bearing intermetallics (Q-phase, $Al_5Cu_2Mg_8Si_6$) with spherical morphology are identified in the microstructure, either with coarser (Q_1, >1 μm) or finer (Q_2, >0.3 μm) dimensions.[13,59,60] The Fe-intermetallics normally grow around pre-existing α-Al dendrite arms, *e.g.*, *via* lateral growth between primary dendrites in case of β-Al_5FeSi intermetallics,[21,22] so that most of them are located at the dendritic boundaries or within the interdendritic regions.

For the alloys 356, A356, and A356 + 0.5Cu (collectively, Al-Si alloys), the microstructures are dendritic and contain intermetallics at the interdendritic boundaries, similar to that for 319 alloy (Figures 5 through 7). The eutectic Si particles are nodular and ~3–5 μm in size; the size distribution of Si particles, however, shows many finer particles of <1 μm. One common feature of these Al-Si alloys is the absence of blocky α-$Al_8(Fe,Mn)_2Si$ phase as opposed to the 319 alloy. Instead, Mn-bearing Fe-intermetallics in elongated and/or irregular morphology (~2–5 μm in length) are present. Although the presence of Mn suggests that these elongated precipitates are not β-Al_5FeSi, it is possible that the structural and morphological transition is not complete for these Al-Si alloys, unlike 319 alloy. This difference is related to the Fe:Mn ratio in the composition which dictates the extent of morphological transformation between β-Al_5FeSi and α-$Al_8(Fe,Mn)_2Si$ by influencing the nucleation rate of these two phases.[24,26,27] The Mn content should be >0.2 wt pct with an ideal Fe:Mn ratio of ~1.2 to cause the near complete conversion of β-Al_5FeSi to α-$Al_8(Fe,Mn)_2Si$.

The Fe:Mn ratio is not appropriately maintained, plus the Mn content is lower than that required theoretically for structural transformation for the low Fe-containing Al-Si alloys, *e.g.*, A356 (0.16 wt pct Fe and 0.06 wt pct Mn; Fe:Mn = ~3) and A356 + 0.5Cu (0.14 wt pct Fe and 0.08 wt pct Mn; Fe:Mn = 1.75) (Table I). For these two alloys, the low Fe content ensures lower volume fraction of β-Al_5FeSi that could possibly affect the castability and therefore does not call for a complete transformation to α-$Al_8(Fe,Mn)_2Si$. The higher Fe-containing alloys, *e.g.*, 319 alloy (0.68 wt pct Fe) and 356 (0.39 wt pct Fe), on the other hand, may render higher volume fraction of Fe-containing intermetallics than the previous two alloys. For these two alloys, a higher level of Mn (0.39 wt pct for 319 and 0.25 wt pct for 356) is added to the composition to ensure the structural transition from β-Al_5FeSi to α-$Al_8(Fe,Mn)_2Si$. Although the Fe:Mn ratio is inappropriate to complete conversion for these two alloys as well (Fe:Mn = 1.74 for 319 and 1.56 for 356), the higher Mn content ensures the formation of 'Chinese script' α-$Al_8(Fe,Mn)_2Si$ precipitates up to certain extent and that improves castability in the presence of Fe.

Finally, a characteristic intermetallic that only forms in Al-Si alloys (for 356 and A356) is the Mg-containing π-phase ($Al_8FeMg_3Si_6$, Figures 5 and 6).[25] This

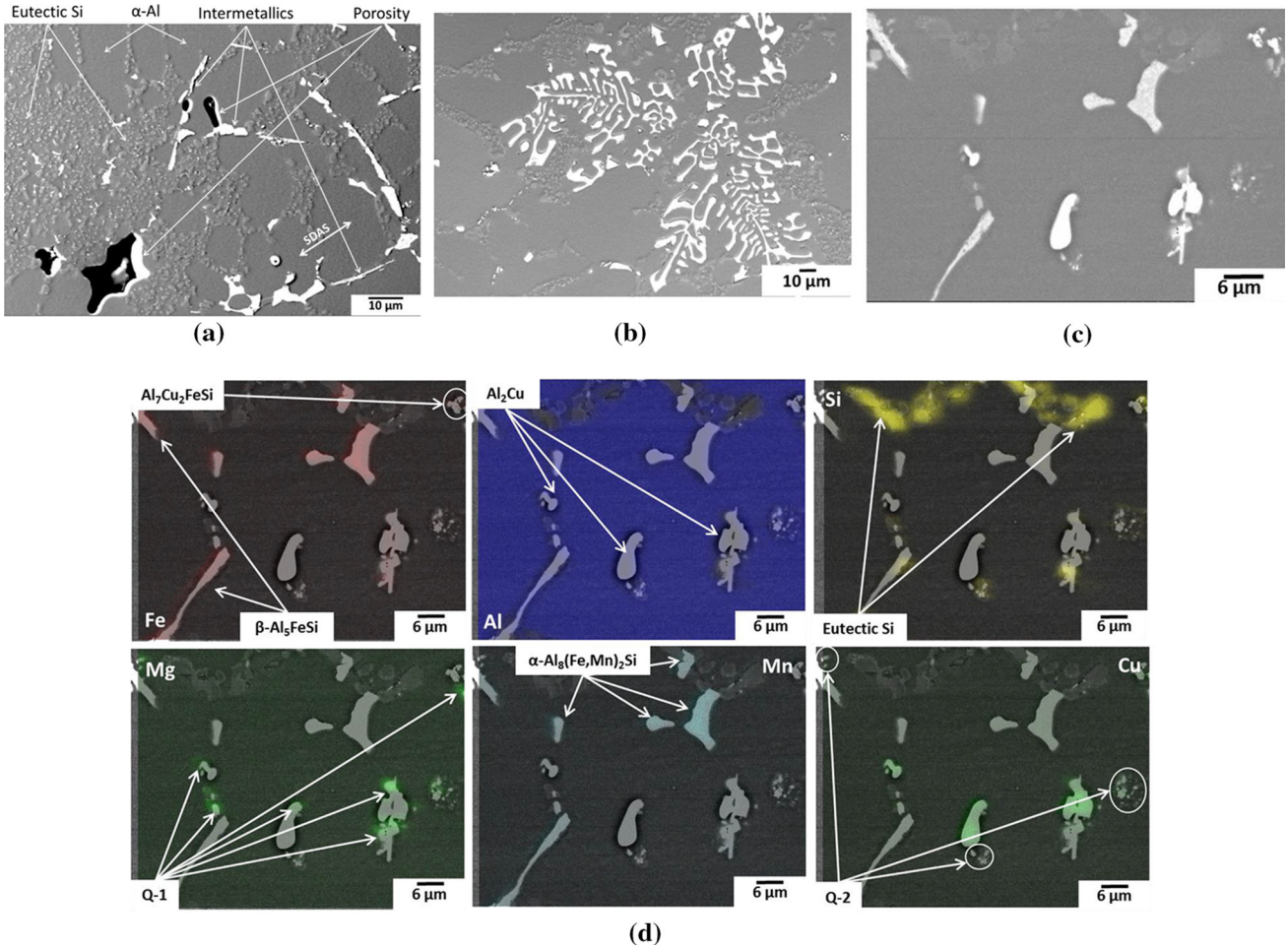

Fig. 4—(*a*) through (*c*) BSE micrographs and (*d*) elemental maps (superimposed with BSE image) obtained from an EDS scan from (c) showing the distribution of various intermetallic precipitates in the microstructure of cast 319 alloy. The elements are inscribed in the corresponding maps; bigger Q-1, and finer Q-2 with spherical morphology are $Al_5Cu_2Mg_8Si_6$.

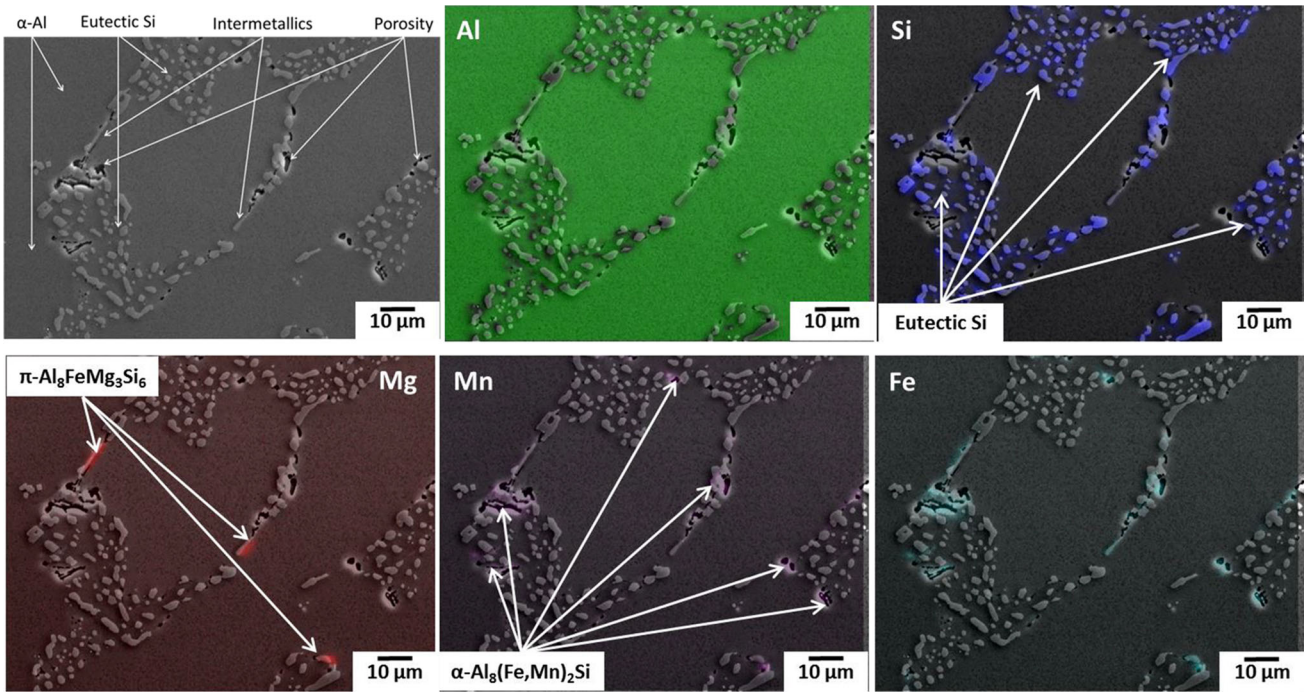

Fig. 5—SE micrograph (top, left) and elemental maps (superimposed with SE image) obtained from EDS scan from corresponding area showing the distribution of various intermetallic precipitates in the microstructure of cast 356 alloy. The elements and various precipitates are inscribed in the corresponding maps.

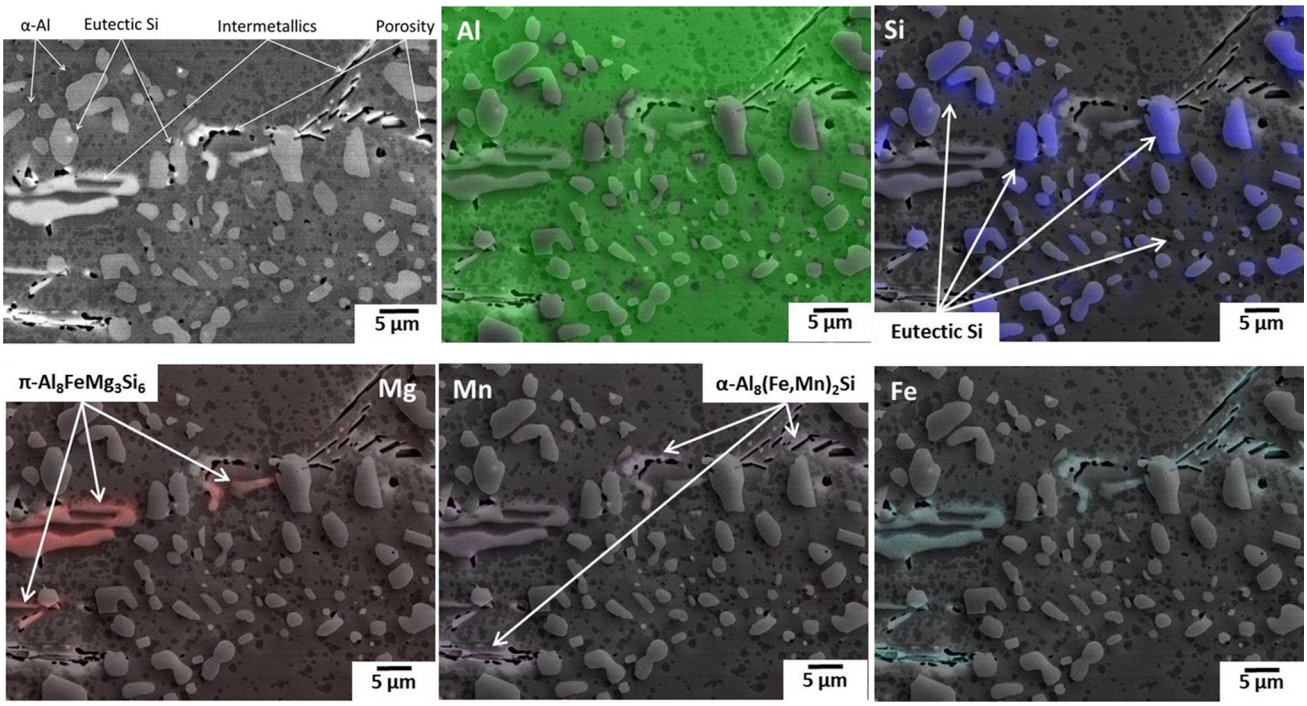

Fig. 6—BSE micrograph(top, left) and elemental maps (superimposed with BSE image) obtained from EDS scan from corresponding area showing the distribution of various intermetallic precipitates in the microstructure of cast A356 alloy. The elements and various precipitates are inscribed in the corresponding maps.

π-phase appears in elongated morphology (~5–10 μm in length and 1–2 μm in width) for both 356 and A356 alloys. The absence of Cu in the composition of 356 or A356 alloys leads to π-phase formation instead of Cu-containing Al_2Cu or Q-$Al_5Cu_2Mg_8Si_6$ phases normally found in Al-Cu (206) or Al-Si-Cu (319) alloy.[14] Table IV summarizes various intermetallic phases with their size/morphology for different cast alloys.

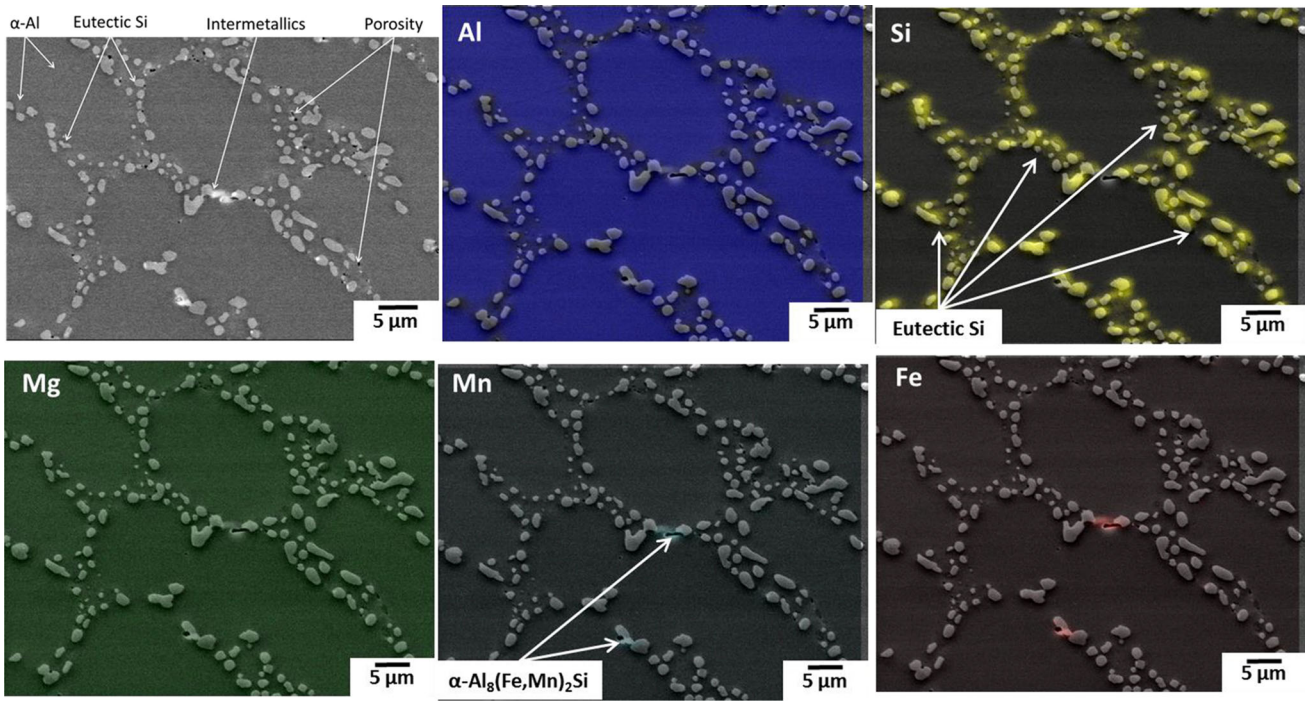

Fig. 7—BSE micrograph (top, left) and elemental maps (superimposed with BSE image) obtained from EDS scan from corresponding area showing the distribution of various intermetallic precipitates in the microstructure of cast A356 + 0.5Cu alloy. The elements and various precipitates are inscribed in the corresponding maps.

3. *X-ray diffraction characterization*

Confirmation of various phases in the microstructure is obtained from the X-ray diffraction of the as-aged alloys (Figure 8). As expected, the principal phase in the XRD profile is the α-Al for all the alloys. Due to the coarse microstructure in the casting and resultant crystallographic texture after solidification, the observed intensity distribution of the α-Al phase is non-random for the dendritic alloys (319, 356, A356, and A356 + 0.5Cu), which is not unexpected.[61] The second major phase in the Al-Si-Cu or Al-Si alloys is the eutectic Si phase, which unlike α-Al phase possesses a smaller grain sizes and a more random orientation.

Other than these major phases, the XRD profiles of the as-aged alloys also indicate several intermetallic phases, which are discussed in Section III–A–2. The peaks corresponding to these intermetallics have lower intensity due to their low volume fractions.[16,62,63] There were several intermetallic phases identified in all the alloys. The 206 alloy possesses ω-Al_7Cu_2Fe and one or two unidentified phases. The 319 alloy has two intermetallic phases identified, α-$Al_8(Fe,Mn)_2Si$ and θ-Al_2Cu with two more possible phases (Q-$Al_5Cu_2Mg_8Si_6$ and π-$Al_8FeMg_3Si_6$). For both the 356 and A356 + 0.5Cu alloys, one intermetallic phase was observed, α-$Al_8(Fe,Mn)_2Si$. For A356 alloy, one or two possible phases were observed (α-$Al_8(Fe,Mn)_2Si$ and π-$Al_8FeMg_3Si_6$). The peaks corresponding to β-Al_5Fe_2Si were not observed in any of these alloys, possibly because of the lower volume fraction of this phase in the microstructure. XRD results are summarized in Table IV and compared with the SEM–EDS results reported in Section III–A–2.

B. *Porosity in Cast Alloys*

Other than the eutectic Si and various intermetallic phases, the as-aged microstructures of Al-Si-Cu or Al-Si alloys also contain pores, primarily at the dendritic boundaries or in the interdendritic regions. They are recognized as shrinkage porosity to distinguish them from those that form due to oxide inclusions or gas absorption.[9] Such pores are considered detrimental for structural integrity of cast automotive parts,[64] *e.g.*, they may act as stress concentrators during cyclic loading.[65]The number density of pores is much less for Al-Cu alloy (206) which is verified on a statistical basis over a large microstructural area. In case of the alloy 319, the shrinkage pores appear in varying size and morphology; the bigger pores are irregular and often larger than 10–15 μm, while the finer pores are spherical or sometimes elongated and within 2–5 μm size range (Figure 4(a)). The size and morphology of the shrinkage pores in the Al-Si alloys are different from that in the 319 alloy. The pores are predominantly spherical (*e.g.*, in 356, Figure 5) or sometimes elongated (*e.g.*, A356 and A356 + 0.5Cu, Figures 6 and 7) but rarely irregular. The spherical pores are ~2–3 μm in size, while elongated pores are <1 μm in width and of widely varying length. The size and morphology of the shrinkage pores for different alloys are also summarized in Table IV.

Smaller size for the shrinkage pores with primarily spherical morphology in Al-Si alloys as opposed to Al-Si-Cu alloy is related to the difference in Fe content and related intermetallic formation between these alloys. Irrespective of the Al-Si-Cu or Al-Si alloys, the shrinkage pores are often adjacent to the Fe-containing

Table IV. Observed Intermetallic Precipitates in the Microstructure of the As-Aged Alloys *via* SEM–EDS and XRD

	Alloy				
Phase	206	319	356	A356	A356 + 0.5Cu
ω-Al_7Cu_2Fe PDF#4-10-1581§§	XRD: observed EDS: Al-Cu-Fe areas SEM: elongated; ~10–20 μm in length, ~1.5 μm in width	XRD: not observed EDS: Al-Cu-Fe-Si areas SEM: blocky; ~2–5 μm			
α-$Al_8(Fe,Mn)_2Si$ PDF#4-9-3712		XRD: observed EDS: Al-Fe-Mn-Si areas SEM: blocky and/or spherical; ~2–5 μm	XRD: observed EDS: Al-Fe-Mn-Si areas SEM: elongated and/or irregular; ~2–5 μm in length	XRD: possible* SEM & EDS: not observed	XRD: observed EDS: Al-Fe-Mn-Si areas SEM: elongated and/or irregular; ~2–5 μm in length
θ-Al_2Cu PDF#4-1-923	XRD: not observed EDS: Al-Cu areas SEM: Blocky and/or spherical; ~2–6 μm	XRD: observed EDS: Al-Cu areas SEM: blocky and/or spherical; ~2–5 μm			
Q-$Al_5Cu_2Mg_8Si_6$ PDF#4-9-1416		XRD: possible* EDS: Al-Cu-Mg-Si areas SEM: spherical; bigger (>1 μm) or finer (>0.3 μm)		XRD: not observed EDS: Al-Fe-Mg-Si areas SEM: elongated and/or irregular; ~2–5 μm in length	XRD: not observed EDS: Al-Fe-Mn-Si areas SEM: elongated and/or irregular; ~2–5 μm in length
π-$Al_8FeMg_3Si_6$ PDF#1-89-971		XRD: possible* SEM & EDS: not observed	XRD: not observed EDS: Al-Fe-Mg-Si areas SEM: elongated; ~5–10 μm in length and 1–2 μm in width	XRD: possible* EDS: Al-Fe-Mg-Si areas SEM: elongated; ~5–10 μm in length and 1–2 μm in width	
Unidentified phases	XRD: 1 or 2 possible			XRD: 1	XRD: 1 possible
Shrinkage pores		SEM: irregular (>10–15 μm) or spherical/ elongated (~ 2–5 μm)	SEM: predominantly spherical (~2–3 μm), occasionally elongated (<1 μm in width)	SEM: spherical (~2–3 μm) or elongated (<1 μm in width)	SEM: spherical (~2–3 μm) or elongated (<1 μm in width)

*Speculative identification based on a non-optimum pattern fit: small number of peaks (<3) with low intensities.

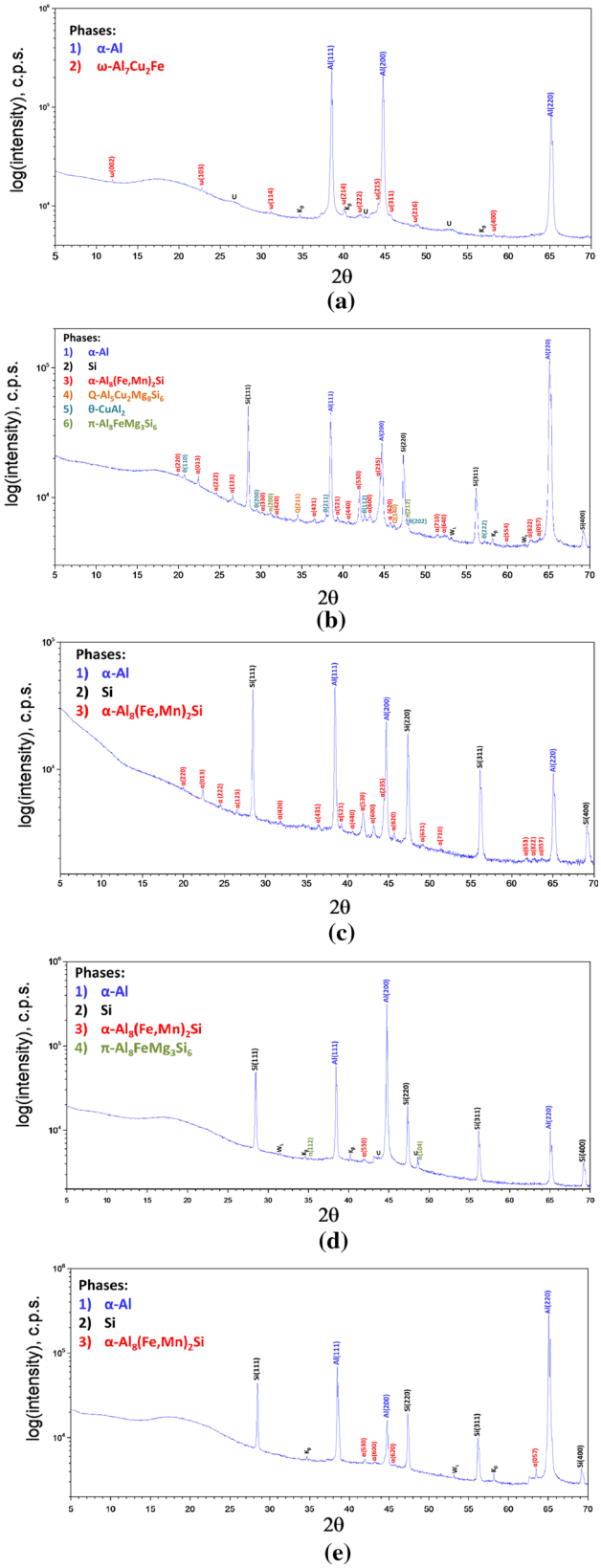

◀Fig. 8—X-ray diffraction profiles of various cast alloys, (*a*) 206, (*b*) 319, (*c*) 356, (*d*) A356, and (*e*) A356 + 0.5Cu identifying major and minor phases present in the microstructure. Intensity in the y-axis is expressed in logarithmic scale. For each phase, the peaks are labeled with the appropriate Miller indices corresponding to the (hkl) for each crystallographic phase. The amorphous hump at low angle originates from the mounting epoxy. Peaks corresponding to Tungsten target L-emission (W_L) and source Cu K_β emission are also labeled. Some unidentified peaks are labeled as 'U.'.

elongated intermetallic phases. These pores form during the last stages of solidification due to insufficient liquid filling within the interdendritic regions.[10] The β-Al_5FeSi intermetallics, because of their elongated, plate-like 3D-structure, are particularly responsible for shrinkage porosity formation since they effectively block the interdendritic channels and reduce the shrinkage feeding.[66] A morphological and structural conversion of β-Al_5FeSi to α-$Al_8(Fe,Mn)_2Si$ is crucial for reducing the pore density in the castings.[11] Shrinkage pores grow preferentially along the surface of the β-Al_5FeSi compared to the α-$Al_8(Fe,Mn)_2Si$ due to the lower gas (entrapped inside the pores)–solid interfacial energy in case of the former intermetallic phase. As already discussed, formation of elongated β-Al_5FeSi intermetallics is not favored for Al-Si alloys (except for 356) in large quantity due to their low Fe content. In contrast, β-Al_5FeSi intermetallics in high volume fraction are likely to form for the Al-Si-Cu alloy 319 with higher Fe content. Also, complete conversion of β-Al_5FeSi to α-$Al_8(Fe,Mn)_2$ is difficult because of the inappropriate Fe:Mn ratio in the latter alloy. Altogether, the absence of elongated β-Al_5FeSi in Al-Si alloys ensures that the shrinkage pores are comparatively finer, spherical, and less in number compared to the Al-Si-Cu (319) alloy.

C. *Nanostructure of the As-aged alloys (TEM observations)*

Figure 9 shows the representative STEM HAADF images of the as-aged alloys (206, 319, and A356). Such images were used to determine the size, morphology, and number density of the nanoscale precipitates. In case of the Al-Cu (206) or Al-Si-Cu (319) alloys, the primary nanoscale strengthening precipitates are θ''or θ' which form on the $\{001\}_{Al}$ habit planes and are made of Al and Cu atoms. The HAADF images in the $\langle 001\rangle_{Al}$ zone axis orientation show two sets of mutually orthogonal plate-shaped precipitates. The Cu atomic columns appear bright and Al atomic columns appear in darker contrast in the HAADF images, in which elemental contrast varies approximately as $(Z_{Cu}/Z_{Al})^{1.7}$.[47] It is to be noted that the length and width of the precipitates in these STEM images represent the actual width and thickness, respectively, of the original plate-shaped θ''or θ' precipitates, while the number density does not account for the third precipitate variant.[67]

The Al-Cu alloy 206 after aging is characterized by a high number density of fine and closely spaced precipitates; the average width is 20–30 nm (Figure 9(a) left). High-magnification image shows the precipitates having the θ''structure, consistent with the Al_3Cu crystallography,[40] in which a pair of planes of Cu atoms is separated by three planes of Al atoms, and satisfying the $\langle 001\rangle\theta''$ || $\langle 001\rangle$Al orientation relationship (Figure 9(a) right). Also seen were numerous single Cu atomic planes

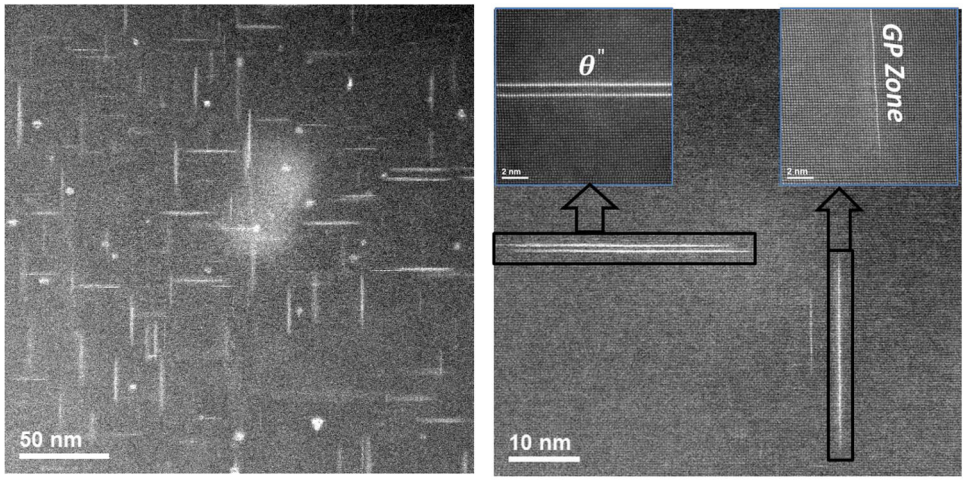

(a)

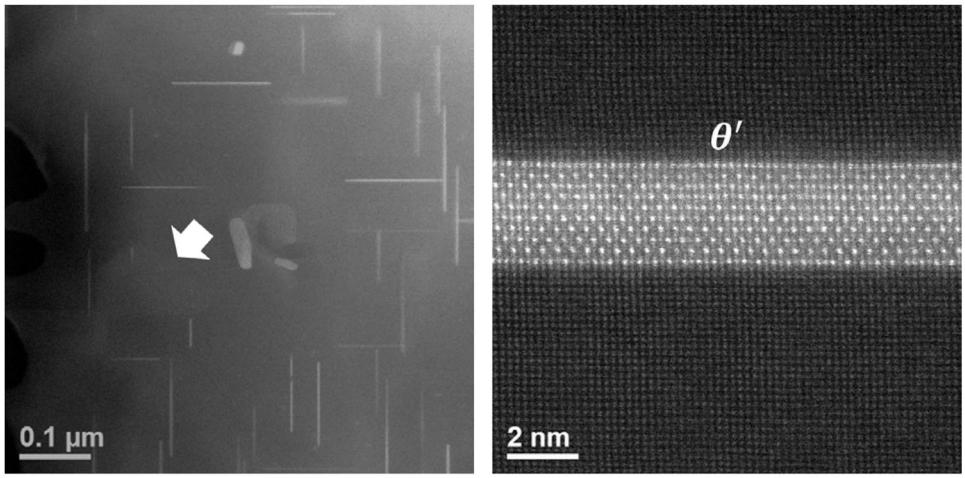

(b)

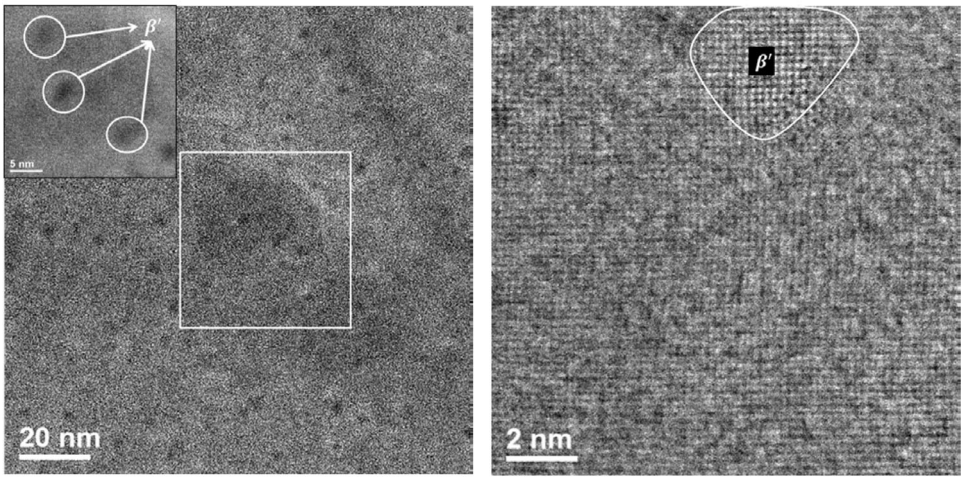

(c)

Fig. 9—HAADF-STEM micrographs at lower magnification (left) and high magnification (right) for (*a*) 206, (*b*) 319, and (*c*) A356. For (a) and (b), θ'' and θ' precipitates appear in bright and α-Al matrix in dark contrast at the low magnification (left side images). At high magnification (with near atomic resolution), the Cu atoms appear in bright and Al atoms in dark contrast. For (c), β' precipitates appear in darker contrast in the bright-field images at low magnification (left side image). The zone axis for is $\langle 001 \rangle_{Al}$ for all these micrographs.

in the nanostructure which are Guinier–Preston zones (GPI). The third set of both θ''or GPI being normal to the electron beam was not distinctly seen because of insufficient scattering by the low number of Cu atoms along the beam direction.

The strengthening precipitate structure in the 319 alloy is shown in Figure 9(b), right. These precipitates have the θ'-Al_2Cu structure, with the (100)Al || (100)θ' and [001]Al || [001]θ' orientation relationship.[38] The number density of θ' precipitates in 319 alloy is much lower compared to that for θ''or GPI in the 206 alloy. The precipitates are characterized by an average width of ~100–150 nm (Figure 9(b): left). The θ'precipitates have thicknesses in the range of 2.5–5 nm; at this thickness, the third habit of the precipitate, normal to the electron beam, is seen in faint bright contrast in the low-magnification image (Figure 9(b) left, marked with arrow).

Figure 9(c) represents the nanoscale precipitates in one of the Al-Si alloys (A356) after aging. These precipitates appear in darker contrast in the low-magnification bright-field images (Figure 9(c) left). This precipitate is distinctly different from the nanoscale θ''or θ' precipitates in the 206 or 319 alloys which appear bright in the background of the α-Al matrix. This difference seems justified considering that the precipitates in the latter two alloys contain Cu with higher atomic number (Z), whereas the A356 alloy forms precipitates with low Z-contrast elements Mg and Si.[68] Furthermore, the nanoscale precipitates in A356 are of circular morphology when viewed along the $\langle 001 \rangle_{Al}$ zone axis as opposed to the plate-shaped θ'' (206) or θ' (319) precipitates. The high-magnification image in the inset, however, suggests that the precipitates are not completely circular and rather of irregular morphology. Most of these precipitates are ~2–5 nm in diameter which is similar to the thickness of the θ' precipitates in 319. An even higher magnification image with near atomic resolution shown in Figure 9(c) right suggests that these precipitates are coherent with the α-Al matrix in the $\langle 001 \rangle_{Al}$ direction. Comparing this precipitate structure and lattice spacing with that reported for similar precipitates in the Al-Mg-Si system,[41,68–70] it is confirmed that they are β' with hcp crystal structure (a = 4.07 Å, c = 4.05 Å). Such precipitates grow as rods or fine needles with $\langle 001 \rangle_{Al}$ as their growth direction and therefore, appear circular when viewed from $\langle 001 \rangle_{Al}$ zone axis.[69,71] Implications of the observed nanostructures for the mechanical and thermal properties of these alloys are reported in Part 2 of this manuscript.[72]

IV. SUMMARY AND CONCLUSIONS

In this part of the present study, candidate cast aluminum alloys for engine cylinder heads from the Al-Cu (206), Al-Si-Cu (319), and Al-Si (356, A356, and A356 + 0.5Cu) alloy systems were studied. The micro- and nanostructure of these alloys was evaluated in the as-aged condition on a comparative basis. The following conclusions are drawn:

1. Equiaxed grain structure for Al-Cu (206) alloy after casting results from grain refinement. The respective size of the dendritic structure for Al-Si-Cu or Al-Si alloys is indicative of the difference in the respective Si content.
2. The presence of Mn causes morphological conversion between β-Al_5FeSi and α-$Al_8(Fe,Mn)_2Si$ for 319 and A356 alloys with higher Fe content. This conversion is however not complete for these two alloys due to inappropriate Fe:Mn ratio.
3. Shrinkage pores hardly form in the equiaxed Al-Cu alloy as opposed to the dendritic Al-Si-Cu or Al-Si alloys. Such pores are comparatively finer and more spherical in morphology for Al-Si alloys than Al-Si-Cu alloy due to an effective conversion of β-Al_5FeSi to α-$Al_8(Fe,Mn)_2Si$ in Al-Si alloys, which helps in liquid filling in interdendritic regions.
4. At the nanoscale, fine coherent GPI and θ'' precipitates form with high number density in 206, while coarse semi-coherent θ' precipitates characterize the 319 alloy. In the Al-Si alloys (A356), nanoscale β' precipitates form as fine needles along $\langle 001 \rangle$Al direction.

ACKNOWLEDGMENTS

Research sponsored by the Propulsion Materials Program, DOE Office of Vehicle Technologies. This research was performed under a Cooperative Research and Development Agreement (CRADA) between ORNL, Nemak, and FCA US LLC. The authors acknowledge Dongwon Shin (ORNL), Christopher Glaspie (FCA), Gregg Black (FCA), and Seyed Mirmiran (FCA) for reviewing the manuscript. This manuscript has been authored by UT-Battelle, LLC under Contract No. DE-AC05-00OR22725 with the U.S. Department of Energy. The United States Government retains and the publisher, by accepting the article for publication, acknowledges that the United States Government retains a non-exclusive, paid-up, irrevocable, world-wide license to publish or reproduce the published form of this manuscript, or allow others to do so, for United States Government purposes. The Department of Energy will provide public access to these results of federally sponsored research in accordance with the DOE Public Access Plan (http://energy.gov/downloads/doe-public-access-plan).

REFERENCES

1. T. Kobayashi: *Strength and Toughness of Materials*, Springer, Tempaku, 2004, pp. 141–61.
2. J.G. Kaufman, E.L. Rooy, and A.F. Society: *Aluminum Alloy Castings: Properties, Processes, and Applications*, ASM International, Materials Park, 2004.

3. M. Javidani and D. Larouche: *Int. Mater. Rev.*, 2014, vol. 59, pp. 132–58.
4. M.D. Peres, C.A. Siqueira, and A. Garcia: *J. Alloys Compd*, 2004, vol. 381, pp. 168–81.
5. Y. Shi, Y. Zhang, Q. Xu, B. Liu, and H. Cui: *IOP Conf. Ser.*, 2012, vol. 33, p. 012112.
6. J. Zhang, Z. Fan, Y.Q. Wang, and B.L. Zhou: *J. Mater. Sci. Lett.*, 2000, vol. 19, pp. 1825–28.
7. L.Y. Zhang, Y.H. Jiang, Z. Ma, S.F. Shan, Y.Z. Jia, C.Z. Fan, and W.K. Wang: *J. Mater. Process. Technol.*, 2008, vol. 207, pp. 107–11.
8. R.N. Grugel: *J. Mater. Sci.*, 1993, vol. 28, pp. 677–83.
9. J.P. Anson and J.E. Gruzleski: *Mater. Charact.*, 1999, vol. 43, pp. 319–35.
10. C.H. Cáceres, M.B. Djurdjevic, T.J. Stockwell, and J.H. Sokolowski: *Scr. Mater.*, 1999, vol. 40, pp. 631–37.
11. N. Roy, A.M. Samuel, and F.H. Samuel: *Metall. Mater. Trans. A*, 1996, vol. 27, pp. 415–29.
12. A.M. Samuel, J. Gauthier, and F.H. Samuel: *Metall. Mater. Trans. A*, 1996, vol. 27, pp. 1785–98.
13. F.H. Samuel: *J. Mater. Sci.*, 1998, vol. 33, pp. 2283–97.
14. E. Sjölander and S. Seifeddine: *J. Mater. Process. Technol.*, 2010, vol. 210, pp. 1249–59.
15. E. Sjölander and S. Seifeddine: *Metall. Mater. Trans. A*, 2014, vol. 45, pp. 1916–27.
16. H. Tanihata, T. Sugawara, K. Matsuda, and S. Ikeno: *J. Mater. Sci.*, 1999, vol. 34, pp. 1205–10.
17. T. Sivarupan, J.A. Taylor, and C.H. Cáceres: *Metall. Mater.Trans. A*, 2015, vol. 46, pp. 2082–2107.
18. K. Liu, X. Cao, and X.G. Chen: *Metallurgical and Materials Transactions A*, 2013, vol. 44, pp. 3494–503.
19. W. Khalifa, F.H. Samuel, and J.E. Gruzleski: *Metall. Mater. Trans. A*, 2003, vol. 34, pp. 807–25.
20. L. Anantha Narayanan, F.H. Samuel, and J.E. Gruzleski: *Metall. Mater. Trans. A*, 1994, vol. 25, pp. 1761–73.
21. C. Puncreobutr, A.B. Phillion, J.L. Fife, P. Rockett, A.P. Horsfield, and P.D. Lee: *Acta Mater.*, 2014, vol. 79, pp. 292–303.
22. C. Dinnis, J.A. Taylor, and A.K. Dahle: *Scr. Mater.*, 2005, vol. 53, pp. 955–58.
23. I. Bacaicoa, M. Luetje, M. Wicke, A. Geisert, F. Zeismann, M. Fehlbier, and A. Brueckner-Foit: *Proc. Struct. Integr.*, 2016, vol. 2, pp. 2269–76.
24. P. Ashtari, H. Tezuka, and T. Sato: *Mater. Trans.*, 2003, vol. 44, pp. 2611–16.
25. G. Gustafsson, T. Thorvaldsson, and G.L. Dunlop: *Metall. Trans. A*, 1986, vol. 17, pp. 45–52.
26. J.Y. Hwang, H.W. Doty, and M.J. Kaufman: *Mater. Sci. Eng.*, 2008, vol. 488, pp. 496–504.
27. S.G. Shabestari: *Mater. Sci. Eng.*, 2004, vol. 383, pp. 289–98.
28. C. Bidmeshki, V. Abouei, H. Saghafian, S.G. Shabestari, and M.T. Noghani: *J. Mater. Res. Technol.*, 2016, vol. 5, pp. 250–58.
29. C.B. Basak and N. Hari Babu: *Mater. Des.*, 2016, vol. 108, pp. 277–88.
30. C.R. Ho and B. Cantor: *J. Mater. Sci.*, 1995, vol. 30, pp. 1912–20.
31. F. Lasagni, B. Mingler, M. Dumont, and H.P. Degischer: *Mater. Sci. Eng.*, 2008, vol. 480, pp. 383–91.
32. J.H. Li, M.Z. Zarif, M. Albu, B.J. McKay, F. Hofer, and P. Schumacher: *Acta Mater.*, 2014, vol. 72, pp. 80–98.
33. L. Qiyang, L. Qingchun, and L. Qifu: *Acta Metall. Mater.*, 1991, vol. 39, pp. 2497–2502.
34. H.R. Shercliff and M.F. Ashby: *Acta Metall. Mater.*, 1990, vol. 38, pp. 1789–802.
35. M. Okayasu, S. Takeuchi, W. Shaohua, and T. Ochi: *J. Mech. Sci. Technol.*, 2016, vol. 30, pp. 1139–47.
36. J.H. Li, J. Barrirero, M. Engstler, H. Aboulfadl, F. Mücklich, and P. Schumacher: *Metall. Mater. Trans. A*, 2015, vol. 46, pp. 1300–11.
37. M. Zamani and S. Seifeddine: *International Journal of Metalcasting*, 2016, vol. 10 (4), pp. 457–65.
38. S.C. Wang and M.J. Starink: *Int. Mater. Rev.*, 2005, vol. 50, pp. 193–215.
39. F.J. Tavitas-Medrano, A.M.A. Mohamed, J.E. Gruzleski, F.H. Samuel, and H.W. Doty: *J. Mater. Sci.*, 2010, vol. 45, pp. 641–51.
40. D.J. Chakrabarti and E. David: Laughlin*Progress Mater. Sci.*, 2004, vol. 49, pp. 389–410.
41. G.A. Edwards, K. Stiller, G.L. Dunlop, and M.J. Couper: *Acta Mater.*, 1998, vol. 46, pp. 3893–3904.
42. M. Murayama and K. Hono: *Acta Mater.*, 1999, vol. 47, pp. 1537–48.
43. M. Murayama, K. Hono, W.F. Miao, and D.E. Laughlin: *Metall. Mater. Trans. A*, 2001, vol. 32, pp. 239–46.
44. C.D. Marioara, S.J. Andersen, J. Røyset, O. Reiso, S. Gulbrandsen-Dahl, T.-E. Nicolaisen, I.-E. Opheim, J.F. Helgaker, and R. Holmestad: *Metall. Mater. Trans. A*, 2014, vol. 45, pp. 2938–49.
45. C.D. Marioara, S.J. Andersen, T.N. Stene, H. Hasting, J. Walmsley, A.T.J. Van Helvoort, and R. Holmestad: *Philos. Mag.*, 2007, vol. 87, pp. 3385–3413.
46. C. Laird and H.I. Aaronson: *Acta Metall.*, 1966, vol. 14, pp. 171–85.
47. R. Yoshimura, T.J. Konno, E. Abe, and K. Hiraga: *Acta Mater.*, 2003, vol. 51, pp. 4251–66.
48. J.D. Boyd and R.B. Nicholson: *Acta Mater.*, 1971, vol. 19, pp. 1379–91.
49. P. Merle and F. Fouquet: *Acta Mater.*, 1981, vol. 29, pp. 1919–27.
50. J. Allison, L. Mei, C. Wolverton, and S. XuMing: *JOM*, 2006, vol. 58, pp. 28–35.
51. P. Huter, P. Renhart, S. Oberfrank, M. Schwab, F. Grün, and B. Stauder: *Int. J. Fatigue*, 2016, vol. 3, pp. 588–601.
52. R. Maniara, L.A. Dobrzański, and J.H. Sokolowski: *J. Achiev. Mater. Manuf. Eng.*, 2007, vol. 17, pp. 217–20.
53. S.G. Shabestari and M. Malekan: *Can. Metall. Quart.*, 2005, vol. 44, pp. 305–12.
54. Q.G. Wang: *Metall. Mater. Trans. A*, 2003, vol. 34, pp. 2887–99.
55. J.G. Kaufman: *Introduction to Aluminum Alloys and Tempers*, ASM International, Materials Park, 2000.
56. N. Ünlü: *Mater. Charact.*, 2008, vol. 59, pp. 547–53.
57. J. da Costa Teixeira, L. Bourgeois, C.W. Sinclair, and C.R. Hutchinson: *Acta Mater.*, 2009, vol. 57, pp. 6075–89.
58. T. Sivarupan, C.H. Caceres, and J.A. Taylor: *Metall. Mater. Trans. A*, 2013, vol. 44, pp. 4071–80.
59. M. Javidani, D. Larouche, and X.G. Chen: *Metall. Mater. Trans. A*, 2016, vol. 30, pp. 4071–80.
60. D.G. Sediako and W. Kasprzak: *Metall. Mater. Trans. A*, 2015, vol. 46, pp. 4160–73.
61. S. Suwas and R.K. Ray: *Crystallographic Texture of Materials*, Springer, London, 2014.
62. J. Sieniawski, G. Mrówka-Nowotnik, and M. Wierzbińska: *Metall. Mater. Trans. A*, 2007, vol. 20, pp. 155–8.
63. N.C.W. Kuijpers, W.H. Kool, P.T.G. Koenis, K.E. Nilsen, I. Todd, and S. van der Zwaag: *Mater. Charact.*, 2002, vol. 49, pp. 409–20.
64. A.R. A, L. Arnberg, E. Fiorese, G. Timelli, and F. Bonollo: *Int. J. Metalcast.*, 2015, vol. 9, pp. 43–53.
65. M. Wicke, M. Luetje, I. Bacaicoa, and A. Brueckner-Foit: *Proc. Struct. Integr.*, 2016, vol. 2, pp. 2643–49.
66. C. Puncreobutr, P.D. Lee, K.M. Kareh, T. Connolley, J.L. Fife, and A.B. Phillion: *Acta Mater.*, 2014, vol. 68, pp. 42–51.
67. J. da Costa Teixeira, D.G. Cram, L. Bourgeois, T.J. Bastow, A.J. Hill, and C.R. Hutchinson: *Acta Mater.*, 2008, vol. 56, pp. 6109–22.
68. K. Matsuda, S. Ikeno, H. Gamada, K. Fujii, Y. Uetani, T. Sato, and A. Kamio: *Metall. Mater.Trans. A*, 1998, vol. 29, pp. 1161–67.
69. J.Y. Yao, D.A. Graham, B. Rinderer, and M.J. Couper: *Micron*, 2001, vol. 32, pp. 865–70.
70. K. Teichmann, C.D. Marioara, S.J. Andersen, and K. Marthinsen: *Mater. Charact.*, 2013, vol. 75, pp. 1–7.
71. L. Ding, Z. Jia, Y. Liu, Y. Weng, and Q. Liu: *J. Alloys Compd.*, 2016, vol. 688, pp. 362–67.
72. S. Roy, L.F. Allard, A. Rodriguez, W.D. Porter, and A. Shyam: *Metall. Mater. Trans. A*, 2017, DOI:10.1007/s11661-017-3986-0.